Microporous and Mesoporous Materials 181 (2013) 233–247

Contents lists available at ScienceDirect

Microporous and Mesoporous Materials

journal homepage: www.elsevier.com/locate/micromeso

Smectite fluorination and its impact on interlayer water content and structure: A way to fine tune the hydrophilicity of clay surfaces?

Baptiste Dazas [a,*], Bruno Lanson [a], Josef Breu [b], Jean-Louis Robert [c], Manuel Pelletier [d], Eric Ferrage [e]

[a] ISTerre, Université Grenoble 1 – CNRS, F-38041 Grenoble Cedex 9, France
[b] Lehrstuhl für Anorganische Chemie I, Universität Bayreuth, D-95440 Bayreuth, Germany
[c] IMPMC, Université Paris 6 – CNRS, F-75252 Paris, France
[d] LIEC, Université de Lorraine – CNRS, F-54501 Vandoeuvre-lès-Nancy Cedex, France
[e] IC2MP – HydrASA, Université de Poitiers – CNRS, F-86022 Poitiers Cedex, France

ARTICLE INFO

Article history:
Received 27 May 2013
Received in revised form 26 July 2013
Accepted 27 July 2013
Available online 2 August 2013

Keywords:
Smectite
Hydrophilicity
Hydrophobicity
Interlayer structure
Anionic substitutions
Smectite-based nanocomposites
Clay heterostructures

ABSTRACT

In addition to isomorphic cation substitutions, smectite layers may present anionic substitutions with fluorine replacing the structural hydroxyl groups and inducing a reduced number of H_2O molecules hydrating interlayer cations. The resulting additional versatility of smectite layers could be used to fine-tune the hydrophilicity of pure or intercalated smectite pending a detailed understanding of interlayer water organization. The present article thus reports on the hydration of (fluoro-)hectorite samples exhibiting similar charge density (structural formulae: $[Na_{0.8}{\cdot}nH_2O]^{inter}[Mg_{5.2}Li_{0.8}]^{oct}[Si_{8.0}]^{tet}O_{20}(OH,F)_4$). Water sorption isotherms and PIGE/PIXE analyses allowed constraining the water content over the probed range of relative humidity and the bulk chemistry, respectively. Modeling of X-ray diffraction (XRD) profiles obtained along water vapor desorption isotherms allowed gaining additional insights in the distribution of interlayer H_2O molecules. Compared to hydroxylated smectites of similar charge, fluorinated hectorites contain ~30% less interlayer H_2O molecules although transitions between discrete hydration states are observed for similar values of relative humidity. These molecules (3–4 and 6–8 H_2O molecules per cation in the mono- and bi-hydrated states, respectively) predominantly belong to the hydration sphere of interlayer cations, although additional H_2O molecules are present in the bi-hydrated state. As a consequence, the positional disorder of interlayer H_2O molecules is much reduced in fluorinated samples, thus increasing the minimum distance from an interlayer H_2O molecule to the smectite layer, most likely owing to the hydrophobicity of fluorinated layers. Finally, the distribution of layers with a given hydration state is more heterogeneous within smectite crystals for fluorinated smectites, compared to hydroxylated ones, possibly as the result of the improved crystallinity.

1. Introduction

Smectite, whose TOT or 2:1 layers include two tetrahedral sheets embedding an octahedral one, represents the most hydrated pole of phyllosilicates. Isomorphic substitutions within both tetrahedral and octahedral sheets induce a permanent layer charge deficit, compensated for by the presence of hydrated cations in the interlayer space. In addition to this significant negative layer charge and related charge-compensating hydrated interlayer cations, its minute crystal size, responsible for large surface areas, makes of smectite a favorable target for molecular engineering to design organic and inorganic hybrid materials, including smectite–polymer nanocomposites and pillared complexes of smectite–metal oxides. In particular, the exchange of smectite interlayer cations by large onium cations resulted in microporous and mesoporous materials with amphiphilic properties [1–3], whereas the ability of smectite to produce a variety of intercalation compounds has been widely used to produce nanocomposites for different applications [4–6]. In addition to isomorphic cation substitutions, smectite layers may present anionic substitutions with fluorine replacing the structural hydroxyl groups, especially for synthetic varieties [7–11]. The presence of structural fluorine induces a significant decrease in the number of H_2O molecules hydrating interlayer cations, as shown by the water vapor sorption isotherms obtained on hydroxylated and fluorinated smectites of similar charge [12–14]. To take advantage of the resulting additional versatility of smectite layers to fine-tune the hydrophilicity of pure or intercalated smectite, a detailed understanding of interlayer water organization is however required.

The present study thus aims at determining the organization of interlayer water in fluorinated and hydroxylated smectites of

* Corresponding author. Tel.: +33 4 76 63 51 95.
E-mail address: baptiste.dazas@ujf-grenoble.fr (B. Dazas).

1387-1811/$ - see front matter © 2013 Elsevier Inc. All rights reserved.
http://dx.doi.org/10.1016/j.micromeso.2013.07.032

similar charge along the water vapor desorption isotherm. Along this isotherm, the stepwise decrease of the apparent layer-to-layer distance experimentally determined with X-ray diffraction (XRD) covers the four crystalline hydration states described previously for smectite [15–18]: tri-hydrated (3W, d_{001} = 18–19 Å), bi-hydrated (2W, d_{001} = 14.9–15.7 Å), mono-hydrated (1W, d_{001} = 11.6–12.9 Å), and dehydrated (0W, d_{001} = 9.7–10.2 Å) smectites. XRD profile modeling allowed taking into account the intrinsic coexistence of layers with contrasting hydration states at given water activity conditions [19–22]. Using additional constraints from water vapor desorption isotherms to quantify the amount of interlayer water, this technique allowed also gaining a detailed insight into the distribution and positional disorder of interlayer H_2O molecules and their relation with charge-compensating cations.

2. Materials and methods

2.1. Sample preparation

Three hectorite samples were synthesized aiming at a common ideal structural formula $[Na_{0.8}]^{inter}[Mg_{5.2}Li_{0.8}]^{oct}[Si_{8.0}]^{tet}O_{20}(F,OH)_4$. The hydroxylated hectorite, hereafter referred to as OH-Hydr, was synthesized hydrothermally from gel precursors in an externally-heated Morey-type pressure vessel with an internal silver tubing [23,24]. Synthesis conditions were 400 °C, 1 kbar P(H_2O), and a duration of four weeks. A fluorinated hectorite sample, hereafter referred to as F-Hydr, was synthesized using a similar hydrothermal procedure. A two-step procedure was used, however, for gel preparation. First, a magnesium depleted gel was prepared, based on the structural formula $[Na_{0.8}]^{inter}[Mg_{3.2}Li_{0.8}]^{oct}[Si_{8.0}]^{tet}O_{20}$, to avoid fluorine depolymerization. Second, the Mg-depleted gel was mechanically mixed with $MgF_{2(solid)}$ to obtain the correct stoichiometry. Finally, sealed gold tubes were used rather than silver tubing to avoid interactions with the metallic vessel. This particular synthesis resulted in the presence of minor quartz (SiO_2), sellaite (MgF_2), and enstatite ($MgSiO_3$) impurities. A second fluorinated hectorite (hereafter referred to as F-HT) was synthesized at high temperature from a melt as described elsewhere, leading to a material with very high homogeneity of layer composition and charge density [10,13,25,26].

All samples were initially sodium-saturated at room temperature by contact with aqueous solutions of NaCl (1 mol/L). Hectorites were shaken mechanically in saline solutions for 24 h before separation of the solid fraction by centrifugation and addition of a fresh saline solution. Four repetitions of these steps ensured a complete cation exchange. Excess sodium chloride was then removed by washing the solid four times by immersion for 24 h in deionized water (Siemens® UltraClear, 18.2 MΩ cm^{-1}).

2.2. Sample characterization

Chemical analysis was performed using ion beam analysis to record simultaneously the signal from all elements present in hectorites and in particular from Li and F, in addition to Si, Mg, Na, O [27,28]. PIGE/PIXE experiments (particle induced gamma- and X-ray emissions, respectively) were conducted with a 3 MeV proton beam at the AGLAE facility (CR2MF, Louvre Museum, Paris – France). Measurements were performed on solid pellets having a 1 cm diameter directly in air with an external microbeam (surface area of 1 mm^2). F and Li concentrations were determined from the gamma emissions integrated at 110 and 197 keV (F) and at 477 keV (Li) and normalization to geostandards (MA-N and DR-N). Concentrations for other elements were calculated from the PIXE spectra using GUPIX.

Water vapor gravimetric desorption isotherms were measured using a lab-built quasi-equilibrium setup designed around a Setaram MTB 10-8 symmetrical microbalance [29]. Water vapor was supplied to the sample (thermostated at 30 °C) from a source kept at 45 °C at a slow flow rate to maintain quasi-equilibrium conditions at all times. Isotherms were deduced from the simultaneous measurements of mass uptake and equilibrium pressure (gauge 0–13.3 kPa). The different samples studied (~100 mg) were initially outgassed at 110 °C for 18 h under a residual pressure of 1 Pa. In addition, N_2 BET surface areas were determined on Na-saturated hydrothermal samples using a Belsorp-Max volumetric gas sorption instrument.

2.3. Methods

Oriented slides were prepared for all three samples by drying at room temperature an aqueous clay suspension on a glass slide. XRD patterns were then recorded using either a Bruker D5000 diffractometer equipped with an Ansyco rh-plus 2250 humidity controller coupled to an Anton Paar TTK450 chamber (F-HT) or a Bruker D8 equipped with a MHG Messtechnik humidity controller coupled to an Anton Paar CHC+ chamber (OH-Hydr, F-Hydr). Intensities were measured with a SolXE Si (Li) solid state detector from Baltic Scientific Instruments for 4 s per 0.04 °2θ step over the 2–50 °2θ CuKα angular range. On the two instruments, the divergence slits, the two Soller slits, the antiscatter, and resolution slits were 0.3°, 2.3°, 0.3°, and 0.1°, respectively. Samples were initially equilibrated at ~97% RH over a saturated $CuSO_4$ solution before being transferred to the chamber, where they were kept at 23 °C under a constant flow of air at the desired RH during the whole data collection. RH was monitored continuously with a hygrometer (uncertainty of ~2% RH) located close to the sample. The dry state was obtained by outgassing the chambers (~10^{-3} Pa) at ambient temperature.

The algorithms developed initially by Drits and co-workers were employed to fit experimental XRD profiles over the recorded 2–50 °2θ CuKα angular range using a trial-and-error approach [30,31]. This approach relies on a user-driven optimization of a structure model aiming at reproducing XRD data. Although this approach precludes taking into account correlations between parameters, owing to the lack of covariance matrix calculation, it has proven successful for the structural characterization of defective and interstratified lamellar structures over the last decades [31,32]. Instrumental and experimental factors such as horizontal and vertical beam divergences, goniometer radius, and length and thickness of the oriented slides were measured and introduced without further adjustment. The mass absorption coefficient (μ^*) was set to 45 cm^2 g^{-1}, as recommended by Moore and Reynolds [33]. Supplementary variable parameters included the layer-to-layer distance. The lognormal distribution of coherent scattering domain sizes along the c^* axis was characterized by a mean value (N), the maximum value being systematically set to 80 layers, the contribution of larger crystals to scattered intensity being negligible because of their low proportion. The z-coordinates of all atoms constituting the 2:1 (or TOT) smectite layer were set as determined previously for hectorites [34]. The interlayer configuration used for 3W layers included two planes of cations on each side of the interlayer midplane. The distance between each of these planes and the interlayer midplane (Δd3W) was refined to ~1.5 Å. Interlayer H_2O molecules were distributed symmetrically above and below these two cationic planes, the interlayer midplane thus hosting twice the number of H_2O molecules present in each of the outer planes. The interlayer configuration used for 2W layers was proposed initially by Ferrage et al. (2005) with one plane of H_2O molecules on each side of the interlayer midplane, that hosts cations [35]. This model was characterized by the distance (Δd2W) between the

interlayer midplane and each of the planes of H_2O molecules. For 1W layers both cations and H_2O molecules were located in the interlayer midplane. A similar configuration was used for 0W layers however without H_2O molecules. The same Debye–Waller temperature factor was used for interlayer cations in all models (B = 5 Å^2) [35]. The actual positional disorder of interlayer cations was not refined further owing to the similar scattering power of Na^+ cations and H_2O molecules, and to the prevalence of the latter species in smectite interlayers. The overall amount of water at a given RH was not considered as a variable parameter in the present work and was constrained by water vapor sorption isotherms, the distribution of this overall amount between the different types of hydrated layers being however refined. N, Δd2W and the Debye–Waller factor of H_2O molecules (B_{wat}) were considered also as variable parameters. The fitting procedure is detailed elsewhere [12,36,37]. The unweighted R_p parameter, which is mainly influenced by fit quality of intense diffraction maxima, was used to quantify the overall fit quality [38].

Except when specifically needed to reproduce a low-angle super-reflection, interstratification of the different types of hydrated layers was systematically random in all mixed layers contributing to the diffracted intensity. The composition of the different mixed layers was however variable, thus leading to an overall segregation of the different layer types. The extent of this segregation can be quantified using the following parameter:

$$\mathrm{Sg(MW)} = 1 - \frac{1 - \left(\frac{\sum_{i=1}^{n} \left[Ab{\cdot}\mathrm{ML}^i \times \left(W^i_{\mathrm{MW}} \right)^2 \right]}{\sum_{i=1}^{n} \left[Ab{\cdot}\mathrm{ML}^i \times \left(W^i_{\mathrm{MW}} \right) \right]} \right)}{1 - \sum_{i=1}^{n} \left[Ab \cdot \mathrm{ML}^i \times \left(W^i_{\mathrm{MW}} \right) \right]} \quad (1)$$

where $Ab{\cdot}\mathrm{ML}^i$ represents the relative proportion of the ith mixed layer contribution, W^i_{MW} the relative abundance in this mixed layer of the major layer type in the sample, and n the total number of mixed layers.

3. Results

3.1. Chemical composition

The element contents determined by PIGE/PIXE and reported in Table 1a were used to calculate structural formulae (Table 1b) for the three hectorites. Al and Ca were not included in the calculation of structural formulae because of their very low contents, sometimes close to detection limits. The systematic presence of quartz (SiO_2) impurity in the samples, revealed by powder XRD (data not shown), prevented the normalization to silicon and structural formulae were thus calculated assuming a total of 6.00 octahedral cations (Mg and Li). The O+OH content was calculated as the difference of the F content to 24 ($O_{20}(OH,F)_4$ basis). The structural formula calculated for F-Hydr used the Mg and Li contents determined experimentally despite the presence of sellaite (MgF_2) and enstatite ($MgSiO_3$) impurities in this sample (2.0% and 0.5%, respectively from quantitative phase analysis using XRD – data not shown). The overall charge of the 2:1 smectite layer is, however, consistent with that calculated for its hydroxylated equivalent (0.69 and 0.72 per O_{20} $(OH,F)_4$, respectively), and perfectly balanced by the number of interlayer cations for both samples. For F-HT, the amount of interlayer Na is significantly increased compared to hydrothermal samples (0.79 compared to 0.69–0.72 per $O_{20}(OH,F)_4$, respectively), thus suggesting a higher charge. The number of structural F in F-HT is also significantly higher than that determined for F-Hydr, consistent with the synthesis conditions.

Table 1
Composition determined by PIGE-PIXE for the hectorites samples (a, weight%), and deduced structural formulae (b, per $O_{20}(OH,F)_4$, see text for details).

	OH-Hydr (%)	F-Hydr (%)	F-HT (%)
(*a*)			
Li	0.68	0.60	0.66
O/OH[a]	47.89	40.45	39.18
F	0.04	7.78	8.74
Na	2.20	2.01	2.36
Mg	17.05	16.35	16.69
Al	0.05	0.05	0.08
Si	32.09	32.71	32.22
Ca	0.00	0.05	0.07
(*b*)			
Si	8.00	8.00	8.00
Mg	5.27	5.31	5.27
Li	0.73	0.69	0.73
Na	0.72	0.69	0.79
O/OH	24.00	20.76	20.47
F	0.00	3.24	3.53
Excess charge	−0.01	0.00	0.06

[a] The amount of O/OH was determined by difference.

3.2. Water vapor desorption isotherms

All water vapor desorption isotherms exhibit similar type IV profiles with the presence of two steps corresponding to domains where bi-hydrated and then mono-hydrated smectite layers dominate (Fig. 1) [39]. Two main types of isotherms may be distinguished however from the content of interlayer H_2O corresponding to the different hydration states, fluorinated smectite containing ~30% less H_2O than its hydroxylated equivalent consistent with results obtained on fluorinated talc [40]. In addition, the transitions between the different hydration domains are much sharper for the F-HT sample compared to hydrothermal ones, consistent with the improved crystallinity of the former sample [34]. For F-HT, the transition between the two domains occurs at ~65% RH and is completed over a 10% RH range, and the plateaus corresponding to the main hydration states are extremely flat, with ~8.0 and 3.95 mmol H_2O per gram of clay over the 2W and 1W domains (92–72% RH, and 60–20% RH, respectively). The amount of H_2O desorbed from F-Hydr is consistent with that in F-HT, but its desorption isotherm is much smoother, consistent with data obtained on natural smectite [41]. Capillary sorption of H_2O molecules at RH values higher than 75% RH, impedes an accurate determination of the 2W domain that appears at first glance to extend from ~90% RH down to 60% RH, with a linear decrease of H_2O from ~9.8 to ~7.1 mmol/g (Fig. 1). The 1W domain extends from 45 to 20% RH, with a linear decrease of interlayer H_2O from ~4.5 to ~3.3 mmol/g. The transition between 2W and 1W states is smoother than for F-HT, spreading over ~15% RH, whereas the 1W/0W transition is similar for the two fluorinated samples with a decrease of the amount of H_2O from ~3.5 mmol/g at ~18% RH to 0.0 mmol/g at 0% RH. Finally the water desorption isotherm measured on OH-Hydr is similar to that of its fluorinated equivalent except for the amount of H_2O which is approximately 50% higher (Fig. 1).

3.3. XRD profile modeling

XRD data and their optimum fits are shown as a function of relative humidity in Figs. 2, 3 and 4, for OH-Hydr, F-Hydr, and F-HT, respectively. The relative proportions of the mixed layers contributing to calculated intensity and their compositions (proportions of the different layer types) are reported in Tables 2–4 for OH-hydr, F-Hydr, and F-HT, respectively. These Tables also include the main structural parameters of crystals (N), layers (layer-to-layer

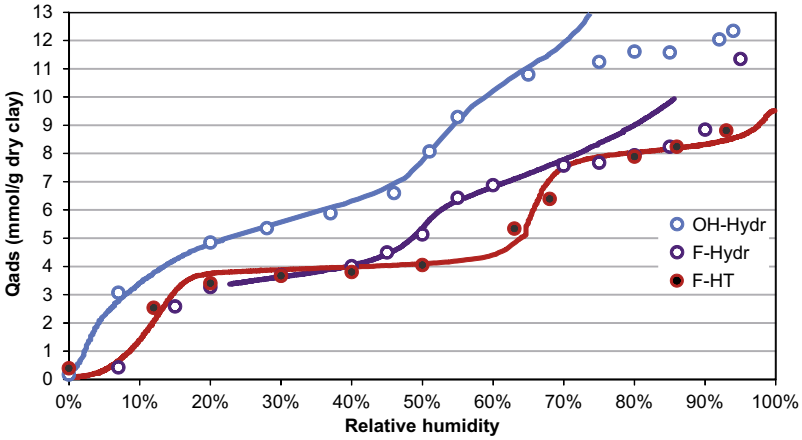

Fig. 1. Smectite water content (Qads) as a function of relative humidity. Solid lines were obtained from water vapor desorption isotherms, whereas dots represent H_2O contents used for XRD profile modeling. Blue, purple, and red patterns represent OH-Hydr, F-Hydr, and F-HT samples, respectively. (For interpretation of the references to color in this figure legend, the reader is referred to the web version of this article.)

distance and its fluctuation – σz, and interlayer H_2O content and organization, with Δd parameters for 2W and 3W layers).

3.3.1. OH-Hydr

From ~98 to 92% RH, XRD patterns were fitted with three mixed layers, the two main ones including mostly or only 2W layers interstratified with minor 3W layers to fit the low-angle asymmetry of the 001 smectite reflection (Fig. 2). The third mixed layer also contains 2W and 3W layers, but exhibits a maximum possible degree of ordering (MPDO) at $R = 1$ (see Drits and Tchoubar for details about mixed-layer nomenclature) [31] and allows reproducing the weak super-reflection at ~2.6 °2θ. Below 92% RH, the super-reflection vanishes and two mixed layers are sufficient to reproduce XRD data. From this RH value down to ~65% RH, the main mixed layer contribution is primarily composed of 2W layers with minor 1W layers to fit the high-angle asymmetry of the 001 smectite reflection, while the minor phase keeps a minor content of 3W layers down to 75% RH. While stable over the 85–65% RH range, the proportion of 1W layers increases significantly at 55% RH as shown by the enhanced high-angle asymmetry of the 001 smectite reflection and by the development of a second order reflection at ~14 °2θ. Accordingly, the contribution of the mixed layer with negligible 1W layers decreases, and two mixed layers with significant or dominant 1W layers are needed to fit the XRD data. At 51 and 46% RH, the relative proportion of 1W layers increases in the three mixed layers required to fit both the broadened 001 smectite reflection and the coexistence of 00l reflections corresponding to both 2W- and 1W-dominated mixed layers. At this point, one of the mixed layers contains essentially 1W layers, whereas 2W layers still dominates another mixed layer. The transition to an essentially mono-hydrated state is complete at 37% RH where two mixed layers are sufficient to fit XRD data. At this RH value, the sample is primarily mono-hydrated, with a minor contribution of 2W layers in the minor mixed layer. Following the desorption isotherm, 2W layers totally disappear at 28% RH, where minor 0W layers are present in one of the two mixed layers. At 20% RH, 1W layers still dominate, with a very similar composition. At 7% RH, the relative contribution of the mixed layer containing essentially 1W layers decreases strongly, consistent with the positional shift of the 001 smectite reflection to higher angles. The emergence of a mixed layer with significant content of 0W layers also contributes to increase the proportion of dehydrated layers. Finally, the pattern recorded at 0% RH is fitted with two mixed layers where 0W prevail, consistent with the almost rational series of 00l reflections ($d_{001} \approx l x d_{00l}$) corresponding to d_{001} = 9.7 Å.

3.3.2. F-Hydr

At 95% RH, the sample is essentially tri-hydrated, consistent with the rationality of 00l reflections corresponding to d_{001} = 18.8 Å. Departure from rationality (ξ), defined as the standard deviation of $l x d_{00l}$ values [42], was calculated to be ~0.024 Å (10 reflections), indicative of a periodic 3W layer stacking. In contrast with this simple picture, four contributions were necessary to fit the pattern recorded at 90% RH. The presence of reflections typical for 3W and 2W smectites (Fig. 3) required the presence of periodic or mixed layer contributions corresponding to these two hydration states, whereas two additional mixed layers with prevailing 2W and minor 3W layers allowed fitting subtle profile modulations. From 85% to 70% RH, one periodic 2W contribution coexists with a mixed layer with prevailing 2W and minor 3W layers, the content of the latter layers decreasing steadily with RH. At 85% and 80% RH, a third mixed layer with prevailing 3W layers is necessary to fit the low-angle shoulder of the smectite 001 reflection. The transition between bi- and mono-hydrated states occurs from 60% to 30% RH. This transition is characterized by a heterogeneous hydration behavior of F-Hydr and the presence of four contributions to the diffracted intensity. The relative contribution of the initially periodic 2W smectite decreases steadily with decreasing RH, as the content of 1W layers increases at the expense of 2W ones. Simultaneously, the relative contribution of a mixed layer with prevailing 1W and minor 2W layers increases together with its content in 1W layers. One of the two mixed layers necessary to fit the XRD data collected over this transition zone has intermediate composition between the previous two, 2W and 1W layers prevailing at 60 and 40% RH, respectively. The last contribution to the data is dominated by 1W layers over the whole transition, these layers coexisting with minor 2W layers at first and next with a marginal amount of 0W layers. Compared to 40% RH, the compositions of the four mixed layers used to fit the XRD data at 30% RH logically contain more 1W layers, the contribution of the only mixed layer still dominated by 2W layers being marginal. The transition to the mono-hydrated state is achieved. At 20% RH, all four mixed layers needed to fit the data are dominated by 1W layers, with the presence of minor 0W layers in the main contribution to account for the high-angle asymmetry of the smectite 001 reflection. When decreasing further the RH to 15%, the relative proportion of 0W layers in this dominant mixed layer increases as indicated by the positional shift of the smectite 001 reflection. At 7% RH, the transition from mono-hydrated to dehydrated state is essentially realized, although a significant proportion of 1W layers is present

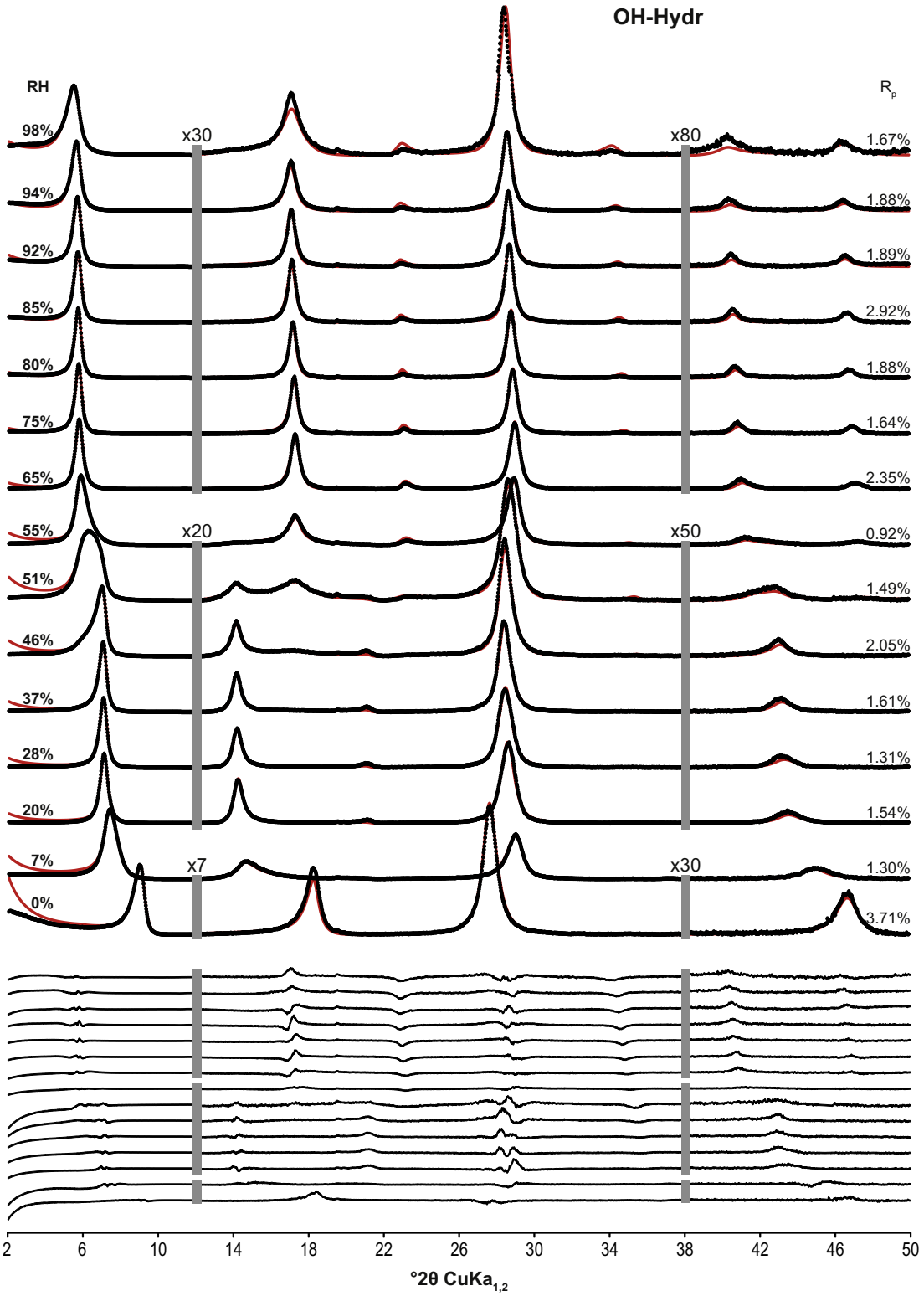

Fig. 2. Comparison between experimental and calculated XRD patterns as a function of relative humidity for OH-Hydr. Experimental and calculated XRD patterns are shown as crosses and solid lines, respectively. Difference plots are shown at the bottom of the figure. The vertical gray bars indicate a modified scale factor for the high-angle regions compared to the 2–10 °2θ angular range. The goodness of fit parameter *R*p is indicated for each pattern.

in two of the four mixed layers needed to fit the data to account for the low-angle asymmetry of the smectite 001 reflection at 9.91 Å. One of the mixed layers with similar contents of 0W and 1W layers exhibits MPDO at $R = 1$ and allows reproducing the super-reflection at ~3.8 °2θ. When decreasing further the RH to 0%, the content of 1W layers in these two mixed layers decreases together with their relative contribution, thus increasing the symmetry of the smectite 001 reflection.

3.3.3. F-HT

From 93% to 80% RH, the sample is essentially bi-hydrated, consistent with the rationality of 00*l* reflections corresponding to a

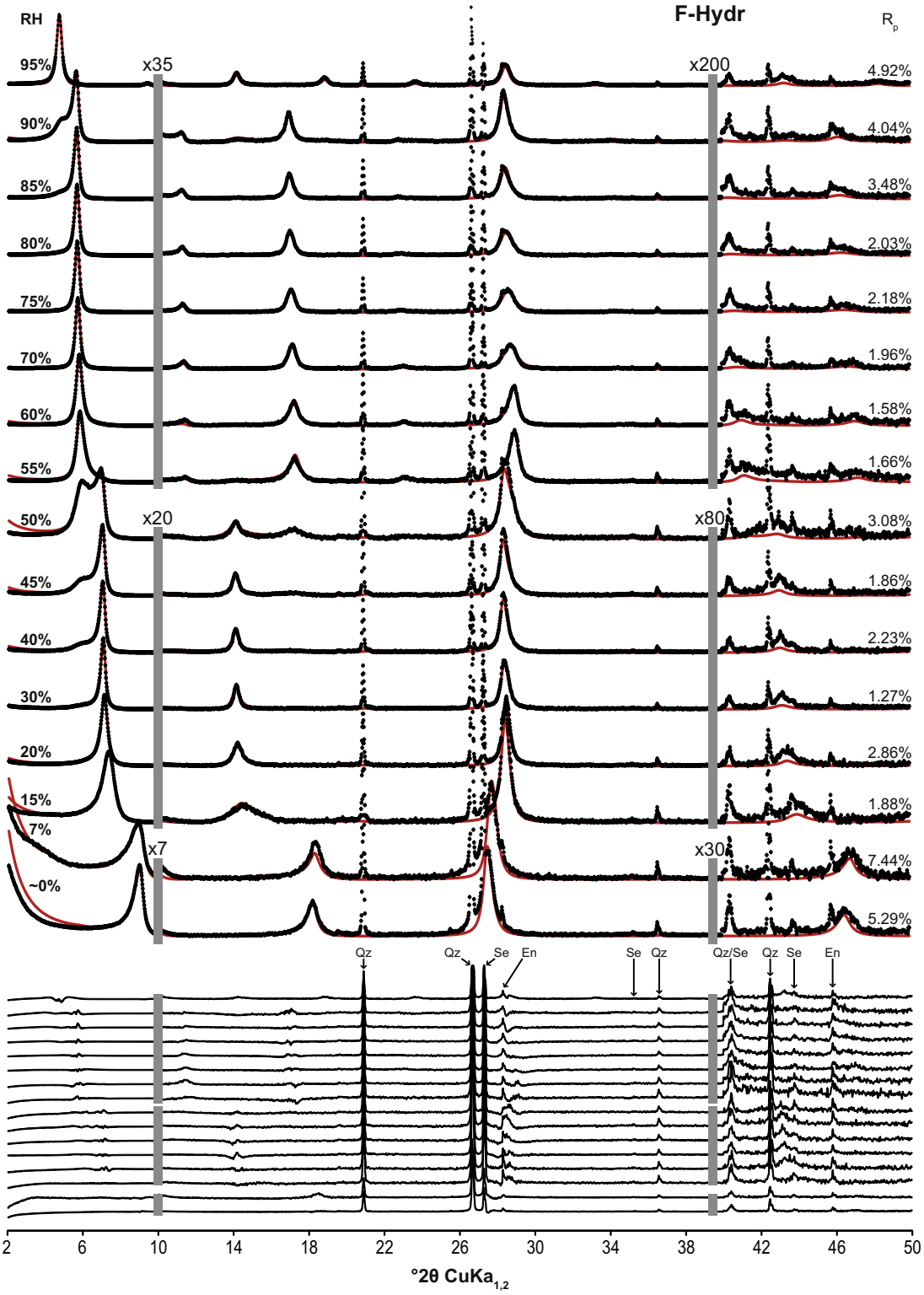

Fig. 3. Comparison between experimental and calculated XRD patterns as a function of RH for F-Hydr. Patterns as for Fig. 2. Diffraction lines from quartz (SiO_2), sellaite (MgF_2), and enstatite ($MgSiO_3$) impurities are indicated as Qz, Se, and En, respectively.

$d_{001} \approx 15.3$–15.4 Å, the ξ parameter being equal to 0.032 Å (8 reflections), 0.036 Å (8 reflections), and 0.103 Å (7 reflections) at 93, 86, and 80% RH, respectively. Accordingly, only 2W layers are present at 93% RH. Diffraction maxima broaden significantly however as the diffraction angle increases and a doublet is actually visible above 40 °2θ, even after subtraction of the $K\alpha_2$ contribution (Fig. 4), indicating the presence of 2W layers with distinct layer-to-layer distances (15.33 and 15.46 Å, respectively, at 93% RH). The different 2W layer types are segregated in distinct crystallites. At 86% RH, crystallites with the two types of 2W layers interstratified with minor 1W layers still dominate the sample. A third, minor, mixed layer with 30% of 1W layers allows fitting weak peak tails. At 80% RH, four mixed layers were considered to fit the diffraction data. The main one contains essentially 2W layers,

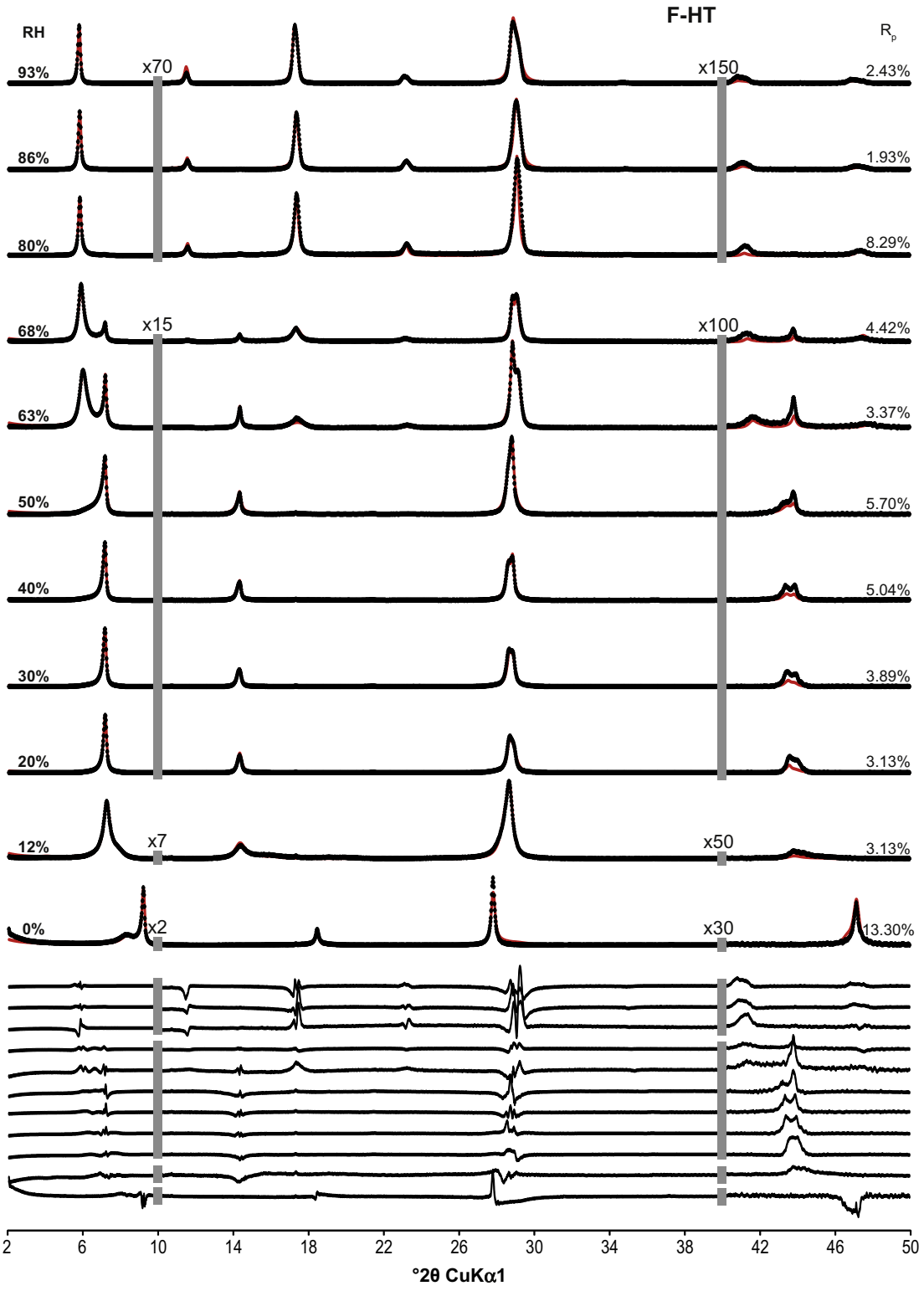

Fig. 4. Comparison between experimental and calculated XRD patterns as a function of RH for F-HT. Patterns as for Fig. 2.

whereas the other two contain both 2W and 1W layers in contrasting proportions (78:22 and 25:75, respectively). All 2W layers exhibit the same layer-to-layer distance. Finally, a minor contribution corresponding to periodic 1W crystals allows fitting the weak peaks of mono-hydrated smectite. From 68% to 63% RH, the relative contribution of periodic 1W smectite increases together with the relative proportion of 1W layers in the three mixed layer contributions. Two types of 1W layers with distinct layer-to-layer distances coexist in the sample, however in different crystallites. At 50% RH, the transition to mono-hydrated smectite is almost complete and the diffraction pattern is dominated by a rational series of 00*l* reflections corresponding to 1W smectite (Fig. 4). A periodic 1W contribution accounts for this series of reflections, whereas two mixed layers dominated by 1W layers

Table 2
Structural parameters used to fit experimental XRD patterns of OH-Hydr as a function of relative humidity.

	RH	98	94	92	85	80	75	65	55	51	46	37	28	20	7	0
Layer-to-layer distance (Å)	0W									9.80	9.70	9.70	9.70	9.70	9.70	9.70
	1W				12.90	12.90	12.90	12.90	12.57	12.59	12.57	12.56	12.53	12.47	12.20	12.00
	2W	15.65	15.61	15.59	15.56	15.51	15.45	15.39	15.35	15.29	15.25	14.98				
	3W	18.86	18.80	18.50	18.30	18.20	18.00									
Number of interlayer H_2O molecules[a]	1W				4.55	4.55	4.55	4.55	4.55	4.55	4.48	4.40	4.20	3.90	3.15	2.50
	2W	9.40	9.30	9.20	9.00	8.90	8.70	8.50	8.20	8.10	8.00	8.00				
	3W	12.00	10.50	9.00	8.40	8.10	7.50									
Debye–Waller factor of interlayer H_2O[b]	1W				2	5	5	5	14	43	48	50	50	49	50	50
	2W	50	50	43	39	45	39	28	49	45	50	50				
	3W	38	10	10	10	24	16									
Additional parameters[c]	Δd2W (Å)	1.50	1.50	1.47	1.43	1.49	1.41	1.37	1.40	1.43	1.35	1.05				
	Δd3W (Å)	1.50	1.50	1.50	1.50	1.50	1.50									
	σz (Å)	0.15	0.19	0.20	0.15	0.18	0.20	0.22	0.22	0.20	0.22	0.27	0.30	0.30	0.19	0.22
	σ^* (°)	2.3	4.2	4.4	4.5	4.2	4.3	4.4	4.3	4.2	4.0	3.9	3.6	3.5	4.0	3.3
Phase 1[d]	*Ab.* (%)	0.49	0.75	0.73	0.83	0.79	0.76	0.74	0.33	0.28	0.53	0.88	0.85	0.78	0.15	0.25
	0W (%)										0.01	0.01			0.05	1.00
	1W (%)				0.02	0.02	0.02	0.02	0.59	0.90	0.98	0.99	1.00	1.00	0.95	
	2W (%)	0.87	0.96	1.00	0.98	0.98	0.98	0.98	0.41	0.10	0.01					
	3W (%)	0.13	0.04													
	CSD size	6.5	7.1	7.4	7.7	8.6	9.0	8.0	5.6	8.0	9.3	9.3	9.6	9.5	10.8	12.7
Phase 2	*Ab.* (%)	0.46	0.23	0.19	0.17	0.21	0.24	0.26	0.36	0.27	0.38	0.12	0.15	0.21	0.57	0.70
	0W (%)												0.15	0.20	0.24	0.93
	1W (%)							0.10	0.27	0.65	0.76	0.76	0.85	0.80	0.76	0.07
	2W (%)	0.70	0.75	0.80	0.80	0.90	0.90	0.90	0.73	0.35	0.24	0.24				
	3W (%)	0.30	0.25	0.20	0.20	0.10	0.10									
	CSD size	4.0	5.0	4.5	5.0	4.2	5.0	5.5	8.6	9.0	7.3	5.8	8.7	10.5	10.0	8.9
Phase 3	*Ab.* (%)	0.05	0.02	0.08					0.31	0.45	0.09			0.01	0.28	0.05
	0W (%)									0.06				0.40	0.40	0.50
	1W (%)								0.04	0.27	0.32			0.60	0.60	0.50
	2W (%)	0.50	0.50	0.50					0.96	0.67	0.68					
	3W (%)	0.50	0.50	0.50												
	CSD size	2.0	1.4	1.4					7.6	6.5	6.5			10.0	8.0	2.0

[a] The number of interlayer H_2O molecules is given per $O_{20}(OH,F)_4$ for each layer type.
[b] Debye–Waller factor of interlayer H_2O is given in $Å^2$ for each layer type.
[c] Δd : distance, in projection along the c* axis, between the interlayer midplane and the maximum density of the H_2O molecule distribution. σz : Standard deviation of layer thickness. σ^* : Standard deviation of the distribution of particles orientation.
[d] The relative abundance (*Ab.*), the composition (proportion of the different layer types), and the size of coherent scattering domains (CSD) are given for each contribution to the simulated diffraction pattern. Average CSD size is given in layers per crystal.

allow fitting the low-angle shoulder of the 001 reflection. A fourth mixed layer with equivalent contents of 1W and 2W layers is also present. At this stage of the dehydration, the two types of 1W layers coexist within the same crystallites. The same mixed layers are present down to 20% RH, dehydration inducing both the steady decrease of the most hydrated mixed layers and the progressive increase of their 1W layer content. At 20% RH, two periodic 1W smectites, each with a distinct layer-to-layer distance, account for about 2/3 of the sample, whereas the third contribution contains ~5% of 2W layers interstratified with 1W ones. The coexistence of two types of 1W layers is evidenced by the progressive peak broadening and splitting with increasing diffraction angles, even after subtraction of the $K\alpha_2$ contribution (Fig. 4). At 12% RH, the main contribution is still dominated by 1W layers although strong peak tails indicate the presence of 0W layers in all four mixed layers required to fit the data. Under vacuum, dehydrated layers prevail in the four contributions. Three of these mixed layers contain more than 80% of 0W layers. The distinct reflection on the low-angle side of the 001 reflection (Fig. 4) is characteristic of the fourth mixed layer which contains equivalent amounts of 0W and 1W layers.

4. Discussion

4.1. Evolution of smectite hydration

The profile modeling approach used in the present study allows gaining precise insights into the overall hydration of the investigated smectites despite their heterogeneity. In particular, by plotting the relative proportions of the different layer types as a function of RH (Fig. 5) it is possible to determine the actual position of the transition between different hydration domains and to assess hydration homogeneity. Plots obtained for both hydroxylated and fluorinated hydrothermal smectites are consistent with those obtained on synthetic smectite of equivalent charge but exhibiting tetrahedral substitutions (saponite S-$Na_{0.8}$) [12]. Plateaus corresponding to bi-hydrated and mono-hydrated states are clearly visible over most of the RH range investigated, and the dehydration of 2W smectite occurs at ~50% RH. At low RH values, both samples are dominated by 0W layers, consistent with results obtained on saponite with similar layer charge [12]. Despite this overall consistency, minor differences occur between the samples, although hectorite and saponite were obtained with

Table 3
Structural parameters used to reproduce experimental patterns of F-Hydr as a function of RH.

	RH	95	90	85	80	75	70	60	55	50	45	40	30	20	15	7	0
Layer-to-layer distance (Å)	0W										9.80	9.80	9.75	9.75	9.75	9.69	9.75
	1W							12.60	12.60	12.60	12.60	12.59	12.56	12.50	12.45	12.40	12.40
	2W		15.72	15.68	15.64	15.59	15.53	15.43	15.39	15.34	15.28	15.25	15.20	15.20	15.20		
	3W	18.81	18.80	18.79	18.70	18.55	18.40										
Number of interlayer H_2O molecules	1W							3.15	3.00	3.00	2.95	2.90	2.78	2.60	2.55	2.50	2.50
	2W		5.98	5.96	5.90	5.82	5.78	5.66	5.56	5.40	4.80	4.40	4.40	4.40	4.40		
	3W	8.70	8.49	8.40	8.25	8.10	7.95										
Debye–Waller factor of interlayer H_2O	1W							5	5	5	13	6	5	5	5	50	50
	2W		5	8	11	7	6	18	14	50	5	5	5	5	5		
	3W	10	50	11	12	5	5										
Additional parameters	Δd2W (Å)		1.43	1.43	1.44	1.47	1.48	1.50	1.50	1.48	1.36	1.25	1.05	1.05	1.50		
	Δd3W (Å)	1.50	1.50	1.48	1.44	1.38	1.29										
	σz (Å)	0.25	0.25	0.31	0.38	0.40	0.39	0.25	0.22	0.20	0.20	0.22	0.24	0.18	0.10	0.05	0.12
	σ^* (°)	15.0	5.7	5.8	4.5	4.3	3.9	5.0	6.0	5.8	6.0	4.8	4.9	8.0	10.5	15.0	20.0
Phase 1	*Ab.* (%)	1.00	0.26	0.62	0.79	0.79	0.74	0.44	0.38	0.19	0.12	0.07	0.03	0.26	0.04	0.42	0.28
	0W (%)															0.80	0.85
	1W (%)							0.02	0.05	0.12	0.16	0.20	0.30	0.95	0.90	0.20	0.15
	2W (%)		1.00	0.99	0.99	0.99	1.00	0.98	0.95	0.88	0.84	0.80	0.70	0.05	0.10		
	3W (%)	1.00		0.01	0.01	0.01											
	CSD size	8.1	13.4	12.5	12.5	12.9	11.8	11.1	10.7	6.9	5.9	4.0	5.7	12.0	7.0	14.8	15.0
Phase 2	*Ab.* (%)		0.27	0.25	0.14	0.21	0.26	0.45	0.45	0.19	0.19	0.17	0.16	0.14		0.03	0.03
	0W (%)															0.50	0.70
	1W (%)							0.12	0.22	0.50	0.66	0.70	0.90	0.90		0.50	0.30
	2W (%)		0.88	0.85	0.85	0.90	0.95	0.88	0.78	0.50	0.34	0.30	0.10	0.10			
	3W (%)		0.12	0.15	0.15	0.10	0.05										
	CSD size		12.0	10.0	11.0	11.0	11.0	7.8	7.9	7.9	9.1	5.0	8.7	6.1		6.1	15.0
Phase 3	*Ab.* (%)		0.27	0.13	0.07				0.09	0.39	0.21	0.29	0.16	0.32	0.04	0.07	0.06
	0W (%)										0.02	0.02	0.03	0.15	0.40	1.00	1.00
	1W (%)								0.57	0.80	0.98	0.98	0.97	0.85	0.60		
	2W (%)		0.15	0.23	0.23				0.43	0.20							
	3W (%)		0.85	0.77	0.77												
	CSD size		4.5	4.5	4.5				7.6	7.5	20.0	23.0	27.6	27.3	10.0	15.0	5.0
Phase 4	*Ab.* (%)		0.20					0.11	0.08	0.23	0.48	0.47	0.65	0.28	0.92	0.48	0.63
	0W (%)												0.02	0.03	0.23	0.94	0.97
	1W (%)							0.80	0.93	0.95	0.95	0.95	0.95	0.97	0.77	0.06	0.03
	2W (%)		0.70					0.20	0.07	0.05	0.05	0.05	0.03				
	3W (%)		0.30														
	CSD size		7.0					4.2	5.7	15.0	12.3	14.0	19.8	19.9	11.7	13.2	15.0

the same synthesis protocol [12,23]. First, hectorite samples contain a significant amount of 3W layers at high RH values. These layers are actually predominant in F-Hydr that exhibits a rational series of 00*l* reflections corresponding to a d_{001} = 18.8 Å. Despite minor imperfections (for example at ~43.3 °2θ), the overall fit of the pattern calculated with a strictly periodic 3W structure to the data support the hypothesized structure model for these layers [43–46]. In addition, the proportion of 3W layers remains significant in hectorite down to ~80–85% RH. The absence of 3W layers in saponite is unlikely due to the experimental conditions as maximum RH values obtained with both this sample and F-Hydr were similar. The absence of 3W layers in saponite under high RH conditions is more likely due to the location of isomorphic substitutions in the tetrahedral sheets that leads to stronger interactions between the interlayer cations and the 2:1 layers. The transition from bi- to mono-hydrated state occurs at ~50% RH for the two hydrothermal hectorites. 2W layers persist however over a much extended range in F-Hydr compared to OH-Hydr and saponite. In the latter samples, the relative proportion of 2W layers is marginal at ~30% RH, compared to ~15% RH for F-Hydr. This specific behavior will be discussed further in the section devoted to the structure of interlayer H_2O. Finally, dehydration occurs below ~15% RH for F-Hydr, which dehydrates more readily than hydroxylated samples whose dehydration begins below ~10% RH (Figs. 5a and b; Fig. 3 in Ferrage et al. [37]).

The overall hydration behavior of F-HT slightly differs from that of hydrothermal hectorites. No 3W layers were detected in F-HT and the 2W–1W transition occurs at higher RH values (~65% RH – Fig. 5c), despite the higher layer charge deficit of this sample (~0.8 per $O_{20}(OH,F)_4$) compared to hydrothermal ones (~0.7 per $O_{20}(OH,F)_4$) [37]. In addition, the transition spreads over a slightly extended RH range (~35% RH) compared to hydrothermal samples. On the other hand, the 1W–0W transition appears shifted towards lower RH values compared to F-Hydr.

4.2. Dehydration mechanism

As shown previously [42,47], statistical description of layer stacking may yield information on the actual reaction mechanisms affecting smectite interlayers. In the present case, a segregation parameter can be calculated for the prevailing layer along the desorption isotherms (Fig. 6). This parameter may vary from 0,

Table 4
Structural parameters used to reproduce experimental patterns of F-HT as a function of RH.

	RH	93	86	80	68	63	50	40	30	20	12	0
Layer-to-layer distance (Å)	0W										9.63	9.63
	1W			12.53	12.61	12.60	12.49	12.48	12.46	12.45	12.41	11.80
	1Wb[a]		12.40	12.42	12.38	12.38	12.38	12.38	12.37	12.37		
	2W	15.33	15.30	15.32	15.31	15.24	15.15	15.05	15.00	14.90		
	2Wb[a]	15.46	15.37									
Number of interlayer H_2O molecules	1W		3.35	3.35	3.30	3.00	2.95	2.90	2.68	2.60	2.50	2.50
	1Wb		3.35	3.30	3.00	2.80	2.75	2.70	2.90	2.60		
	2W	6.80	6.56	6.44	6.10	5.70	5.20	4.60	4.40	4.00		
Debye–Waller factor of interlayer H_2O	1W		10	5	7	5	7	5	5	5	5	5
	2W	8	10	5	5	5	50	5	20	5		
Additional parameters	Δd2W (Å)	1.50	1.50	1.31	1.21	1.50	1.50	1.49	1.40	1.40		
	σz (Å)	0.25	0.22	0.12	0.06	0.07	0.12	0.13	0.12	0.12	0.16	0.13
	σ^* (°)	4.0	4.8	8.0	6.0	6.0	3.0	4.0	5.0	4.5	5.0	1.5
Phase 1	*Ab.* (%)	0.52	0.48	0.05	0.20	0.23	0.38	0.35	0.46	0.34	0.51	0.62
	0W (%)										0.09	0.99
	1W (%)						0.78	0.93	0.95	0.95	0.91	0.01
	1Wb (%)		0.01	0.75	0.90	0.90	0.10					
	2W (%)	1.00	0.99	0.25	0.10	0.10	0.12	0.07	0.05	0.05		
	2Wb (%)											
	CSD size	26	26	10	20	15	10	10	13	10	18	45
Phase 2	*Ab.* (%)	0.48	0.47	0.75	0.46	0.32	0.24	0.30	0.16	0.11	0.35	0.15
	0W (%)										0.35	0.80
	1W (%)			0.02	0.09	0.17	0.85	0.96	0.98	1.00	0.65	0.20
	1Wb (%)		0.02				0.13	0.02	0.01			
	2W (%)			0.98	0.91	0.83	0.02	0.02	0.01			
	2Wb (%)	1.00	0.98									
	CSD size	19	21	20	16	15	17	25	30	40	15	15
Phase 3	*Ab.* (%)		0.05	0.02	0.09	0.19	0.27	0.30	0.35	0.55	0.09	0.07
	0W (%)										0.48	0.90
	1W (%)										0.52	0.10
	1Wb (%)		0.30	1.00	1.00	1.00	0.98	0.99	0.99	0.99		
	2W (%)		0.70				0.02	0.01	0.01	0.01		
	2Wb (%)											
	CSD size		19	15	30	30	30	40	35	27	18	45
Phase 4	*Ab.* (%)			0.18	0.25	0.26	0.11	0.05	0.03		0.05	0.16
	0W (%)										0.50	0.53
	1W (%)			0.22	0.32	0.40	0.50	0.55	0.60		0.50	0.47
	1Wb (%)											
	2W (%)			0.78	0.68	0.60	0.50	0.45	0.40			
	2Wb (%)											
	CSD size			7	9	10	8	10	10		8	45

[a] Two types of mono- and bi-hydrated layers (1W and 2W layers, respectively) with different layer-to-layer distances were necessary to fit the XRD data.

for randomly interstratified mixed layers and in a pure periodic phase, to 1, for the physical mixture of two periodic structures. Increasing values are related to the increased probability to find the prevailing layers in crystals primarily composed of this layer type. Over the plateaus with the clear prevalence of one layer type, values of the Sg parameter scatter from 0.0–0.2, consistent with values reported previously for the interstratification of layers with different interlayer cations [42,47]. This parameter increases dramatically however during the transition from one hydration state to the other. For OH-Hydr, Sg parameter reaches ~0.3 during both 3W–2W and 2W–1W transitions, compared to ~0.05–0.10 over homogeneous hydration domains. This sharp increase indicates that dehydration does not occur at random within smectite crystallites and that restricted domains with a predominant hydration state are formed during transitions. The formation of such "homogeneous" domains is strongly enhanced for fluorinated samples with values of Sg parameter equal to 0.4–0.5 over the 3W–2W (F-Hydr) and 2W–1W (F-Hydr and F-HT) transitions. This confirms the qualitative assessment of XRD profiles for these two samples that exhibit clear doublets, distinctive of coexisting homogeneous domains with different hydrations states (Figs. 2 and 3). The origin of this specific behavior remains however unclear as it could arise directly from the fluorination or indirectly, for example through the crystallinity improvement. Crystallinity improvement is demonstrated by the larger sizes of coherent scattering domains determined for fluorinated hectorites compared to hydroxylated ones (Tables 2–4), and by the reduction of BET surface areas determined for F-Hydr compared to OH-Hydr (17.59 and 27.08 $m^2\ g^{-1}$, respectively). The increase in crystal sizes measured for F-Hydr compared to OH-Hydr reduces also the discrepancy between the amount of H_2O sorbed and that of interlayer H_2O under high RH conditions (Fig. 1), the two values being similar for F-HT consistent with large crystal sizes.

Lower values of the Sg parameter are calculated for the 1W–0W transition for all samples, possibly because this transition is less comprehensively described in the present study because of experimental constraints. It should be noted also that for F-Hydr this transition is characterized by the presence of an ordered mixed layer in which similar contents of 0W and 1W layers alternate with MPDO (tendency to form 1W–0W layer sequences), as previously reported [12,42,48].

4.3. Content and organization of interlayer H_2O

Water vapor desorption isotherms obtained on the three hectorites investigated (Fig. 1) indicate a much reduced content of

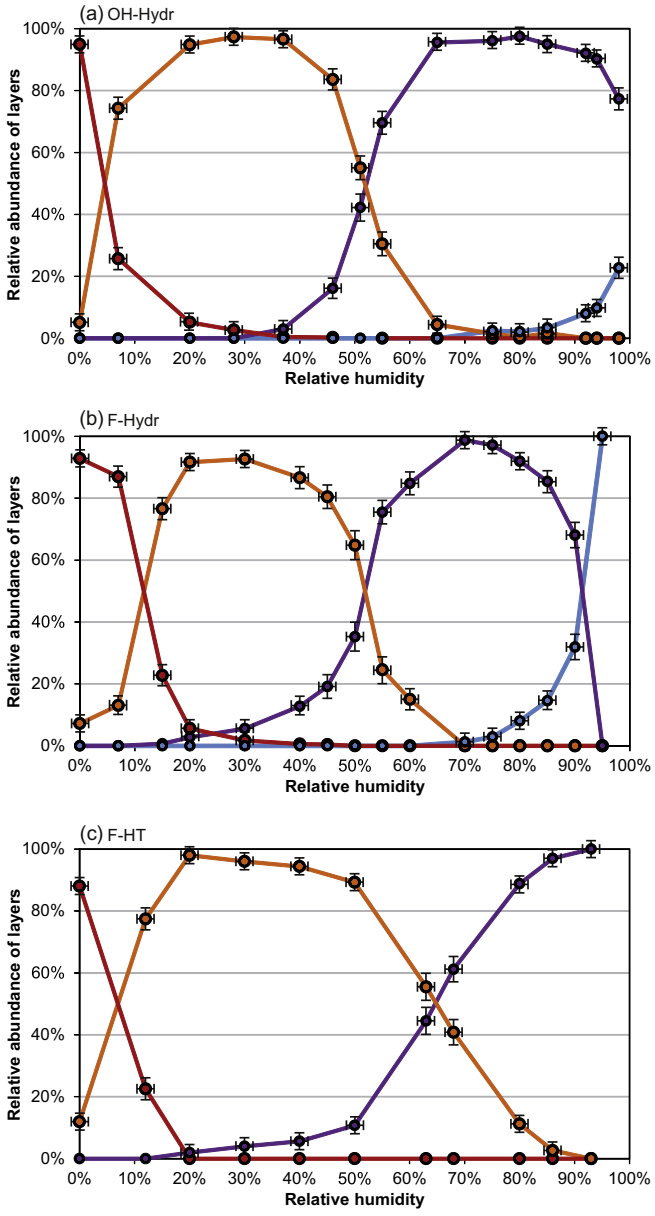

Fig. 5. Evolution of the relative contribution of the different layer types (summing up all contributions to the diffracted intensity) along water vapor desorption isotherms for (a) OH-Hydr, (b) F-Hydr, and (c) F-HT. Blue, purple, orange, and red patterns represent 3W, 2W, 1W, and 0W layers, respectively. The error on RH was estimated to be ±2%, that on layer abundance was considered to vary linearly from ±2% when the relative proportion of a given layer is 100 or 0%, to ±5% when this layer accounts for 50% of the total layers. (For interpretation of the references to color in this figure legend, the reader is referred to the web version of this article.)

interlayer H_2O in fluorinated samples compared to hydroxylated ones. A similar decrease in external water content has been reported for fluorinated, compared to hydroxylated, non-swelling clay minerals (talc) [40], possibly owing to hydrophobic basal surfaces for fluorinated 2:1 clay structures. Taking into account results obtained on hydroxylated saponites and the present results, the influence of charge location (tetrahedral vs. octahedral) and that of structural fluorine on the organization of interlayer H_2O will be assessed in both mono- and bi-hydrated smectites [12].

4.3.1. Mono-hydrated smectite layers

1W layers of OH-Hydr, S-$Na_{0.8}$, and S-$Na_{1.4}$, two hydroxylated saponites with ideal structural formulae $[Na_{0.8}]^{inter}[Mg_{6.0}]^{oct}[Si_{7.2}Al_{0.8}]^{tet}O_{20}(OH)_4$ and $[Na_{1.4}]^{inter}[Mg_{6.0}]^{oct}[Si_{6.6}Al_{1.4}]^{tet}O_{20}(OH)_4$, respectively, contain a similar number of interlayer H_2O molecules, this number decreasing from ~6 to ~3 per $O_{20}(OH)_4$ along the desorption isotherm (Fig. 7a). For a given number of interlayer H_2O molecules, the layer-to-layer distance is ~0.15–0.20 Å higher in OH-Hydr compared to S-$Na_{0.8}$ (Fig. 7a). The observed increase in layer-to-layer distance is about constant over the whole RH range investigated and possibly arises from the reduced electrostatic interactions between the 2:1 layer and the cation owing to the different location of the layer charge deficit between saponite (tetrahedral) and hectorite (octahedral). Consistently, the layer-to-layer distance decreases further when the electrostatic attraction between the 2:1 layer and the cation is increased by increasing the layer charge from 0.8 to 1.4 per $O_{20}(OH)_4$ for a given charge location (S-$Na_{0.8}$, and S-$Na_{1.4}$, respectively – Fig. 7a). The distinct undersaturation of oxygen atoms on the basal surfaces could also be responsible for the absence of 1W OH-Hydr layers with more than 5.0 H_2O molecules per $O_{20}(0H)_4$, the formation of layers with higher hydration states being favored in this case by the weak cation-layer interactions.

As suggested by water vapor sorption isotherms (Fig. 1), the water content is much reduced in fluorinated samples compared to hydroxylated ones, with about 2.5–3.0 H_2O molecules per $O_{20}(OH)_4$ along the isotherm (Fig. 7a). The reduced content of interlayer H_2O in fluorinated samples logically induces a reduced number of H_2O molecules per cation (3.0–4.0 H_2O molecule per cation), this number being comparable to that obtained in high-charge S-$Na_{1.4}$ (Fig. 7b). Molecular modeling simulations indicated that for the latter sample, all H_2O molecules belong to the cation first hydration shell [49]. With increasing RH, the number of H_2O molecules increases and induces a limited evolution of the layer-to-layer distance possibly resulting from the reorganization of the cation hydration shells [50]. Depending on the water content, the hectorite layer-to-layer distance varies from ~12.4 to 12.6 Å, a much reduced range compared to high-charge S-$Na_{1.4}$ [12], likely owing to the reduced density of interlayer species. The layer-to-layer distances determined for fluorinated samples are equivalent to those obtained for most hydrated 1 W OH-Hydr despite the different amounts of interlayer H_2O, most likely as the result of hydrophobic surfaces of fluorinated phyllosilicates [40]. In addition to reducing the number of interlayer H_2O molecules that can be hosted in a given size interlayer, fluorine also reduces the positional disorder of these interlayer species. In the present study, the positional distribution of interlayer H_2O molecules was modeled by using the Debye–Waller parameter (B_{wat}), commonly used to describe thermal motion, the overall H_2O content being constrained by the water vapor desorption data. The B_{wat} parameter can be related to the full width at half maximum intensity (FWHM) of a Gaussian distribution [51], that provides a decent description of interlayer H_2O positional distribution [12,41,42]:

$$\mathrm{FWHM} = \frac{\sqrt{B}\sqrt{\mathrm{Ln}(2)}}{\pi} \quad (2)$$

Over the mono-hydrated domain, that is below 50% RH, FWHM values determined for OH-Hydr (~1.5 Å – Fig. 8) are consistent with those reported for hydroxylated saponites [12]. On the other hand, values obtained for fluorinated hectorites (~0.5 Å) indicate (i) that the positional scattering of these molecules along the *z*-direction is much reduced for fluorinated samples compared to hydroxylated ones, and (ii) that the minimum distance from H_2O molecules to the 2:1 layer is much higher in the former samples, consistent with the considered surface hydrophobicity of fluorinated phyllosilicates.

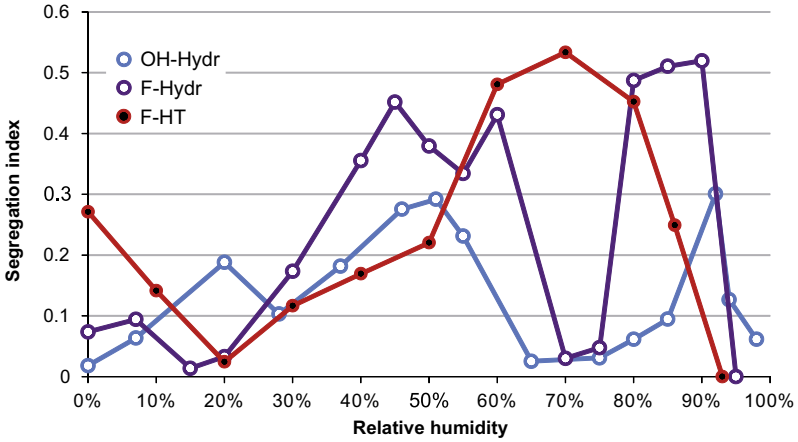

Fig. 6. Segregation index (see text for details) of the main layer type as a function of RH along the desorption isotherm. Patterns as in Fig. 1.

4.3.2. Bi-hydrated smectite layers

2W layers of OH-Hydr, S-$Na_{0.8}$, and S-$Na_{1.4}$ contain a similar number of interlayer H_2O molecules, this number decreasing from ~10 to ~8 per $O_{20}(OH)_4$ along the desorption isotherm (Fig. 9a). Consistent with the increasing electrostatic attraction between the 2:1 layer and interlayer cations, the layer-to-layer distance decreases from OH-Hydr to S-$Na_{0.8}$, and to S-$Na_{1.4}$ for a given number of interlayer H_2O molecules (Fig. 9a).

In addition, the water content is much reduced in fluorinated samples compared to hydroxylated ones, with 4.0–7.0 H_2O molecules per $O_{20}(OH)_4$ along the isotherm, as for mono-hydrated smectite (Fig. 9a). When normalized to the number of interlayer cations, this reduced number of H_2O molecules in fluorinated hectorites is similar to that reported for S-$Na_{1.4}$ (4.5–8.5 and 6.0–7.0 H_2O per cation, respectively – Fig. 9b) [12]. This reduced number exceeds however the number of H_2O molecules from the first cat-

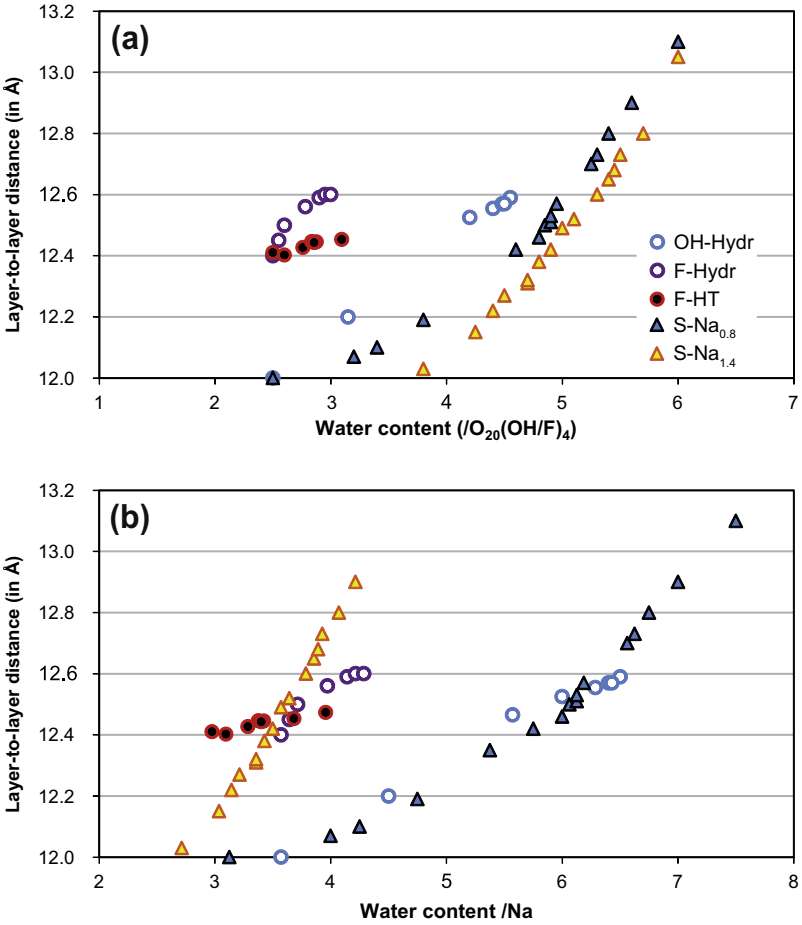

Fig. 7. Evolution of the layer-to-layer distance as a function of interlayer water content for mono-hydrated layers. The number of interlayer H_2O molecules is normalized to $O_{20}(OH,F)_4$ (a) or to the number of interlayer cations (b). Results obtained on S-$Na_{0.8}$ and S-$Na_{1.4}$ by Ferrage et al. [12] are shown as blue and yellow triangles, respectively. Other patterns as in Fig. 1. (For interpretation of the references to color in this figure legend, the reader is referred to the web version of this article.)

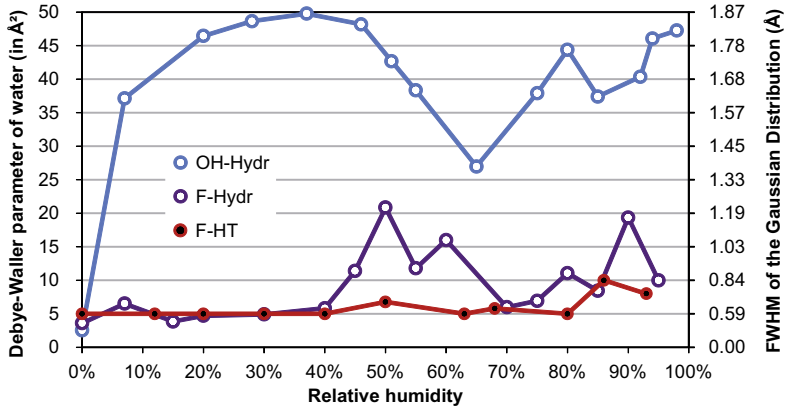

Fig. 8. Evolution of the Debye–Waller parameter (B_{wat}) and of the related FWHM of interlayer H_2O molecules positional distribution as a function of relative humidity. Patterns as in Fig. 1.

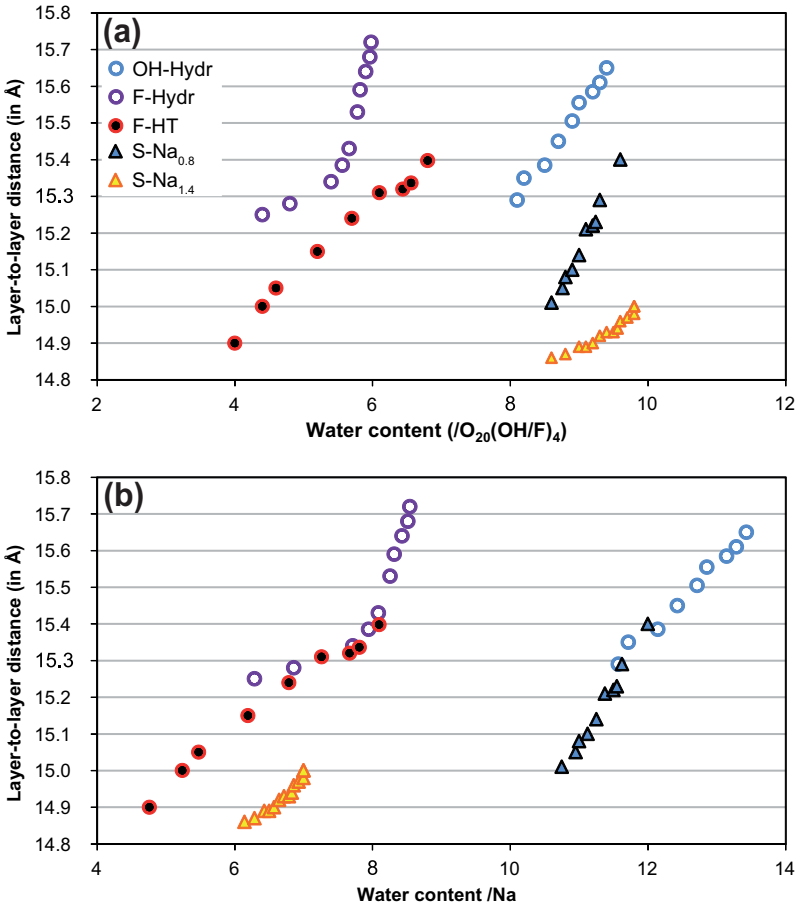

Fig. 9. Evolution of the layer-to-layer distance as a function of interlayer water content for bi-hydrated layers. The number of interlayer H_2O molecules is normalized to $O_{20}(OH,F)_4$ (a) or to the number of interlayer cations (b). Patterns as in Fig. 7.

ion hydration shell (4.0–5.0 H_2O per cation) [49], in contrast to mono-hydrated smectite. Compared to hectorites, the layer-to-layer distance is shorter in S-$Na_{1.4}$, the minimum layer-to-layer distance determined for S-$Na_{1.4}$ despite the higher total number of H_2O molecules arising from interlayer species ordering [37]. Similar low values were obtained for F-HT, whose layer charge and cation distributions are also ordered [34,52]. In addition, for fluorinated smectites and more especially for F-Hydr the layer-to-layer distance increases sharply when increasing the number of interlayer H_2O molecules above ~8.0 H_2O per cation. This increased impact of additional H_2O molecules occurs for numbers of H_2O molecules largely exceeding that of the cation primary hydration shell [49], and likely corresponds to the complete filling of the H_2O molecule "planes". In this case, addition of extra H_2O molecules can be accommodated only by the increase of the layer-to-layer distance owing to the hydrophobicity of the 2:1 layer surfaces. The number of interlayer H_2O molecules and the layer-to-layer distance depends much more on RH in hectorites

than in S-$Na_{1.4}$, however. This likely originates from steric constraints in the high-charge saponite.

Finally, H_2O molecules display similar configurations around interlayer cations in both hydroxylated and fluorinated hectorites with equivalent $\Delta d2W$ values (Tables 2–4), consistent with those reported for saponites [12]. The positional disorder of H_2O molecules is however significantly reduced and the minimum distance from H_2O molecules to the 2:1 layer increased in fluorinated hectorites, as indicated by the reduced B_{wat} parameters over the bi-hydrated domains (Fig. 8). Consistent with 1W layers, these parameters correspond to Gaussian distribution whose FWHM range from ~1.2–1.5 Å in hydroxylated samples to ~0.5–0.75 Å in fluorinated hectorites.

5. Conclusions

Charged fluorinated phyllosilicates exhibit a hydrophobic behavior similar to that previously demonstrated for uncharged clay surfaces. Hydration of charge-compensating interlayer cations remains effective however, although the content of interlayer H_2O is significantly reduced in fluorinated smectite compared its hydroxylated equivalent. For a given layer charge, the content of interlayer H_2O in fluorinated smectite is reduced by ~30% compared to their hydroxylated counterpart as H_2O molecules directly hydrating interlayer cations prevail in the interlayer space of fluorinated smectite. The reduced content of H_2O molecules not bound to interlayer cations is similar to the effect of increased layer charge, although the driving force is likely different (hydrophobicity of 2:1 layer surfaces and steric constraints, respectively). Hydrophobicity of fluorinated smectite surfaces also increases the minimum distance from interlayer H_2O molecules to the 2:1 layer both by increasing the layer-to-layer distance for a given content of interlayer H_2O molecules, compared to hydroxylated smectite, and by reducing the positional disorder of these molecules. For a given content of interlayer H_2O molecules, the layer-to-layer distance depends on the electrostatic interactions between the 2:1 smectite layer and interlayer cations, that is on the amount and location of the layer charge deficit.

The additional versatility of the smectite layer induced by fluorine for hydroxyl anionic substitutions is now to be used to fine-tune the hydrophilicity of pure or intercalated smectite. The contrasting behavior of fluorinated and hydroxylated smectite with respect to water is especially relevant also for the environmental applications of smectite, whose sorption and mechanical properties make an excellent sealant [53]. Owing to experimental constraints, fluorinated smectites have been used indeed to assess water dynamics in clay barriers [13,25,26,54,55]. Additional work, including collation with computational data, is thus required to take into account the distinct structures of interlayer water in both smectite varieties and to estimate the impact of these structural differences on water dynamics.

Acknowlegments

Philippe Walter (CR2MF, Accélérateur Grand Louvre d'Analyse Elémentaire, Paris – France) and Pierre Chansigaud (IC2MP-HydrASA) are thanked for assistance with the PIGE/PIXE analyses, and for BET surface measurements, respectively. The CNRS interdisciplinary "défi" Needs, through its "MiPor" program, and the ANR "Jeunes Chercheurs" program (contract No. ANR-09-JCJC-0106-PorousClay) are thanked for the financial support provided to the present study. The manuscript benefited from the careful comments of three anonymous reviewers.

References

[1] W.L. Ijdo, T.J. Pinnavaia, Chem. Mater. 11 (1999) 3227–3231.
[2] W.L. Ijdo, T.J. Pinnavaia, J. Solid State Chem. 139 (1998) 281–289.
[3] W.L. Ijdo, T. Lee, T.J. Pinnavaia, Adv. Mater. 8 (1996) 79–83.
[4] R.M. Barrer, P.B. Tinker, L. Fowden, Clay Minerals : Their Structure, Behaviour and Use, Royal Society, London, 1984.
[5] S. Sinha Ray, M. Okamoto, Prog. Polym. Sci. 28 (2003) 1539–1641.
[6] S. Pavlidou, C.D. Papaspyrides, Prog. Polym. Sci. 33 (2008) 1119–1198.
[7] M. Reinholdt, J. Miehé-Brendlé, L. Delmotte, M.-H. Tuilier, R. le Dred, R. Cortès, A.-M. Flank, Eur. J. Inorg. Chem. 2001 (2001) 2831–2841.
[8] M. Reinholdt, J. Miehé-Brendlé, L. Delmotte, R. Le Dred, M.-H. Tuilier, Clay Miner. 40 (2005) 177–190.
[9] D. Zhang, C.-H. Zhou, C.-X. Lin, D.-S. Tong, W.-H. Yu, Appl. Clay Sci. 50 (2010) 1–11.
[10] J. Breu, W. Seidl, A. Stoll, K. Lange, T. Probst, Chem. Mater. 13 (2001) 4213–4220.
[11] J. Breu, W. Seidl, J. Senker, Z. Anorg. Allg. Chem. 630 (2004) 80–90.
[12] E. Ferrage, B. Lanson, L.J. Michot, J.-L. Robert, J. Phys. Chem. C 114 (2010) 4515–4526.
[13] N. Malikova, A. Cadène, V. Marry, E. Dubois, P. Turq, J. Phys. Chem. B 110 (2006) 3206–3214.
[14] L.J. Michot, I. Bihannic, M. Pelletier, E. Rinnert, J.-L. Robert, Am. Mineral. 90 (2005) 166–172.
[15] G. Nagelschmidt, Z. Kristallogr. 93 (1936) 481–487.
[16] W.F. Bradley, R.E. Grim, G.L. Clark, Z. Kristallogr. 97 (1937) 216–222.
[17] R.W. Mooney, A.G. Keenan, L.A. Wood, J. Am. Chem. Soc. 74 (1952) 1371–1374.
[18] K. Norrish, Discuss. Faraday Soc. 18 (1954) 120–134.
[19] I. Berend, J.-M. Cases, M. Francois, J.-P. Uriot, L. Michot, A. Masion, F. Thomas, Clays Clay Miner. 43 (1995) 324–336.
[20] J.M. Cases, I. Berend, G. Besson, M. Francois, J.P. Uriot, F. Thomas, J.E. Poirier, Langmuir 8 (1992) 2730–2739.
[21] J.M. Cases, I. Berend, M. Francois, J.P. Uriot, L.J. Michot, F. Thomas, Clays Clay Miner. 45 (1997) 8–22.
[22] J. Cuadros, Am. J. Sci. 297 (1997) 829–841.
[23] D.L. Hamilton, C.M.B. Henderson, Mineral. Mag. 36 (1968) 832–838.
[24] J.-L. Robert, J.-M. Beny, G. Della Ventura, M. Hardy, Eur. J. Mineral. 5 (1993) 7–18.
[25] N. Malikova, A. Cadène, E. Dubois, V. Marry, S. Durand-Vidal, P. Turq, J. Breu, S. Longeville, J.-M. Zanotti, J. Phys. Chem. C 111 (2007) 17603–17611.
[26] V. Marry, E. Dubois, N. Malikova, S. Durand-Vidal, S. Longeville, J. Breu, Environ. Sci. Technol. 45 (2011) 2850–2855.
[27] J.-C. Dran, J. Salomon, T. Calligaro, P. Walter, Nucl. Instrum. Methods B 219–220 (2004) 7–15.
[28] J. Salomon, J.-C. Dran, T. Guillou, B. Moignard, L. Pichon, P. Walter, F. Mathis, Nucl. Instrum. Methods B 266 (2008) 2273–2278.
[29] J.E. Poirier, M. François, J.M. Cases, J. Rouquerol, in: A.I. Liapis (Ed.), Proc. 2nd Eng. Foundation Conf. Fundamental Adsorption, AIChE Pub., New York, 1987, pp. 473–482.
[30] V.A. Drits, B. A. Sakharov, X-ray structural analysis of mixed-layer minerals, Transactions of the Academy of Sciences USSR, vol. 295, Nauka, Moscow, 1976
[31] V.A. Drits, C. Tchoubar, X-ray Diffraction by Disordered Lamellar Structures: Theory and Applications to Microdivided Silicates and Carbons, Springer-Verlag, New York, 1990.
[32] B. Lanson, in: M.F. Brigatti, A. Mottana (Eds.), Layered Mineral Structures and their Application in Advanced Technologies, Eur. Min. Union & Min. Soc.,, . Great Britain & Ireland, London, 2011, pp. 151–202.
[33] D.M. Moore, R.C. Reynolds, X-ray Diffraction and the Identification and Analysis of Clay Minerals, Oxford University Press, Oxford, 1997.
[34] W. Seidl, J. Breu, Z. Kristallogr. 220 (2005) 169–176.
[35] J.F. Burst, AAPG Bull. 53 (1969) 73–93.
[36] E. Ferrage, B. Lanson, N. Malikova, A. Plançon, B.A. Sakharov, V.A. Drits, Chem. Mater. 17 (2005) 3499–3512.
[37] E. Ferrage, B. Lanson, B.A. Sakharov, N. Geoffroy, E. Jacquot, V.A. Drits, Am. Mineral. 92 (2007) 1731–1743.
[38] S.A. Howard, K.D. Preston, Reviews in mineralogy 20: modern powder diffraction, in: D.L. Bish, J.E. Post (Eds.), 20, Min. Soc. Am. Rev. Miner. Geochem., Chantilly, VA, 1989, pp. 217–275.
[39] K. Sing, D. Everett, R. Haul, L. Moscou, R. Pierotti, J. Rouquerol, T. Siemieniewska, Pure Appl. Chem. 57 (1985) 603–619.
[40] L.J. Michot, F. Villieras, M. Francois, J. Yvon, R. Le Dred, J.M. Cases, Langmuir 10 (1994) 3765–3773.
[41] E. Ferrage, B.A. Sakharov, L.J. Michot, A. Delville, A. Bauer, B. Lanson, S. Grangeon, G. Frapper, M. Jimenez-Ruiz, G.J. Cuello, J. Phys. Chem. C 115 (2011) 1867–1881.
[42] E. Ferrage, B. Lanson, B.A. Sakharov, V.A. Drits, Am. Mineral. 90 (2005) 1358–1374.
[43] M. Holmboe, S. Wold, M. Jonsson, J. Contam. Hydrol. 128 (2012) 19–32.
[44] F.R.C. Chang, N.T. Skipper, G. Sposito, Langmuir 11 (1995) 2734–2741.
[45] T.J. Tambach, E.J.M. Hensen, B. Smit, J. Phys. Chem. B 108 (2004) 7586–7596.
[46] L. Tao, T. Xiao-Feng, Z. Yu, G. Tao, Chin. Phys. B 19 (2010) 109101.
[47] E. Tertre, E. Ferrage, I. Bihannic, L.J. Michot, D. Prêt, J. Colloid Interface Sci. 363 (2011) 334–347.
[48] D.M. Moore, J. Hower, Clays Clay Miner. 34 (1986) 379–384.

[49] L.J. Michot, E. Ferrage, M. Jimenez-Ruiz, M. Boehm, A. Delville, J. Phys. Chem. C 116 (2012) 16619–16633.
[50] M. Jiménez-Ruiz, E. Ferrage, A. Delville, L.J. Michot, J. Phys. Chem. A 116 (2012) 2379–2387.
[51] H.D. Shashikala, S.V. Suryanarayana, S.V. Nagender Naidu, J. Appl. Crystallogr. 26 (1993) 602–605.
[52] M.W. Möller, D. Hirsemann, F. Haarmann, J. Sender, J. Breu, Chem. Mater. 22 (2010) 186–196.
[53] W.P. Gates, A. Bouazza, G.J. Churchman, Elements 5 (2009) 105–110.
[54] I. Bihannic, A. Delville, B. Demé, M. Plazanet, F. Villiéras, L.J. Michot, in: L. Liang, R. Rinaldi, H. Schober (Eds.), Neutron Applications in Earth, Energy and Environmental Sciences, Springer, Boston, MA, 2009, pp. 521–546.
[55] L.J. Michot, A. Delville, B. Humbert, M. Plazanet, P. Levitz, J. Phys. Chem. C 111 (2007) 9818–9831.